The Astrophysical Journal, 967:148 (11pp), 2024 June 1 https://doi.org/10.3847/1538-4357/ad3af6

First Extragalactic Detection of Thermal Hydroxyl (OH) 18 cm Emission in M31 Reveals Abundant CO-faint Molecular Gas

Michael P. Busch
Department of Astronomy & Astrophysics, University of California, San Diego, 9500 Gilman Drive, La Jolla, CA 92093, USA; mpbusch@ucsd.edu
Received 2023 November 15; revised 2024 March 21; accepted 2024 April 3; published 2024 May 28

Abstract

The most abundant interstellar molecule, molecular hydrogen (H_2), is practically invisible in cold molecular clouds. Astronomers typically use carbon monoxide (CO) to trace the bulk distribution and mass of H_2 in our galaxy and many others. CO observations alone fail to trace a significant component of molecular gas known as "CO-dark" molecular gas, which can be probed with molecules such as OH and CH. We present an extremely sensitive pilot search for the 18 cm hydroxyl (OH) lines in the Andromeda galaxy (M31) with the 100 m Robert C. Byrd Green Bank Telescope. We successfully detected the 1665 and 1667 MHz OH lines in faint emission. The 1665/1667 MHz line ratio displays the characteristic 5:9 ratio predicted under conditions of local thermodynamic equilibrium. To our knowledge, this is the first detection of nonmaser 18 cm OH emission in another galaxy. We compare our OH and H I observations with archival CO (1–0) observations. Our OH detection position overlaps with the previously discovered Arp Outer Arm in CO. Our best estimates show that the amount of H_2 traced by OH is 100%–140% higher than the amount traced by CO in this sight line. The amount of dark molecular gas implied by dust data supports this conclusion. We conclude that the 18 cm OH lines hold promise as a valuable tool for mapping of the "CO-dark" and "CO-faint" molecular gas phase in nearby galaxies, especially with upcoming multibeam, phased-array feed receivers on radio telescopes, which will allow for drastically improved mapping speeds of faint signals.

Unified Astronomy Thesaurus concepts: Andromeda Galaxy (39); Radio astronomy (1338); Interstellar medium (847); Interstellar clouds (834); Interstellar molecules (849)

1. Introduction

The hydroxyl radical (OH) was the first molecule discovered in the radio regime in absorption toward Cas A 60 yr ago (Weinreb et al. 1963). There was initial optimism at the time that OH would serve as a tracer for the bulk of H_2 in the galaxy. It was quickly discovered that this would be incredibly difficult due to the complex excitation of the four hyperfine structure lines in the lambda doubling ground state (1612, 1665, 1667, and 1720 MHz) and the faintness of the emission signal (Barrett 1967). Surveys for OH in our own Galaxy revealed that measurements of absorption against radio continuum sources were far more successful than those of thermal or quasi-thermal emission due to the typically low excitation temperature (a few K above background continuum and cosmic microwave background radiation, $T_{\rm CMB}$) of the 18 cm OH lines. The first major survey for OH was carried out by Goss (1968) in absorption. Shortly after the discovery of OH 18 cm absorption, Weaver et al. (1965) announced the detection of strong 18 cm lines toward star-forming regions, which turned out to be maser emission from the 1665 and 1667 MHz OH lines. Surveys for OH emission from the OH 18 cm lines over the Galactic plane were unsuccessful with the receiver technology of the time (Penzias 1964), although thermal (or "normal") emission from OH was eventually announced (Heiles 1968). The discovery of the masing phenomenon of OH molecules captured attention as a brighter target for observational OH studies of star-forming regions with single-dish telescopes (Weaver et al. 1965) and interferometers (Rogers et al. 1966) and also of evolved stars (Wilson & Barrett 1968). Meanwhile, millimeter emission from the carbon monoxide (CO) molecule, first detected by Wilson et al. (1970), took over as the choice tracer for probing H_2 in the Galaxy, owing to its brightness and its status as the second-most-abundant molecule after H_2 itself (for reviews, see, e.g., Bolatto et al. 2013; Heyer & Dame 2015). The recent renewed interest in searching for OH emission, both in galactic and extragalactic studies, is partly due to the utility of OH to trace the "CO-dark" (or "CO-faint") molecular gas, a component of the diffuse and translucent molecular clouds in the cold neutral medium where the diffuse molecular gas is not fully traced by CO emission (Allen et al. 2012, 2015; Xu et al. 2016; Li et al. 2018; Busch et al. 2019, 2021). This forms a significant component of the molecular interstellar medium (ISM) and is widely thought to be diffuse H_2, where CO is photodissociated quickly due weaker self-shielding than H_2 (Wolfire et al. 2010).

Attempts to detect nonmaser OH emission in external galaxies have historically been difficult because of the weak strength of the signal and the limitations of receiver technology at the time. The first systematic search for OH in 63 nearby spiral galaxies was led by Schmelz & Baan (1988) using the 305 m Arecibo telescope. There was an early unsuccessful search for high-intensity OH emission from H II regions the Large Magellanic Cloud (LMC) using the Parkes 64 m telescope (Radhakrishnan 1967). The detection of OH maser emission from OH/IR stars in the LMC (Wood et al. 1986) prompted additional searches for OH masers in the Magellanic Clouds (Wood et al. 1992). The now well-known and incredibly bright OH megamaser phenomenon was first discovered in Arp 220 (Baan & Haschick 1987) and was recently revisited with much higher angular resolution data (Baan et al. 2023). Baan et al. (1992) surveyed 321 galaxies for

OH with the NRAO 300 foot telescope, observing six OH megamasers at $z < 0.02$. A large absorption survey of OH in the Magellanic systems is expected to be carried out by the Australian SKA Pathfinder this decade (Dickey et al. 2013). A recent search for OH absorption using the FAST telescope by Zheng et al. (2020) failed to detect any extragalactic OH absorption sources and also reviewed the existing literature on extragalactic OH absorption sources. Of note, one of the earliest searches for extragalactic OH using the Effelsberg 100 m telescope successfully observed thermal OH in absorption in M82 (Mebold et al. 1976). The upgraded Giant Metrewave Radio Telescope has also recently observed OH absorption from a galaxy at $z \sim 0.05$ (Gupta et al. 2018) and carried out an OH absorption survey of many low-z targets (Curran et al. 2017). Gravitational-lens-amplified 1720 MHz OH maser emission had been detected in a system at $z = 0.765$ (Kanekar et al. 2005). Masing 1720 MHz OH emission was also detected in a galaxy at $z = 0.247$ in the MeerKAT Absorption Line Survey (Combes et al. 2021).

The observational discovery of "dark gas," an ISM gas phase seemingly not traced by H I or CO but implied to exist by indirect total gas tracers like γ-rays and dust (Grenier et al. 2005; Wolfire et al. 2010; Planck Collaboration et al. 2011), prompted others to consider the OH emission as a tracer for a diffuse molecular gas phase not traced by CO. This gas phase has since been shown to be primarily molecular gas (Murray et al. 2018; Liszt & Gerin 2023a). It was originally discovered by Wannier et al. (1993) that OH emission can arise at cloud edges, where no corresponding CO emission was detected. The first modern and sensitive blind search for OH emission from the quiescent ISM by Allen et al. (2012) demonstrated that OH emission was ubiquitous and commonly not accompanied by CO emission. A wealth of research has also demonstrated the existence of "CO-dark" molecular gas: the [C II] 158 μm line has been used to trace the "CO-dark" H_2 (Pineda et al. 2013; Bigiel et al. 2020; Chevance et al. 2020; Madden et al. 2020; Schneider et al. 2023), simulations of molecular cloud formation and photodissociation region modeling on cloud and galactic scales (Nickerson et al. 2019; Seifried et al. 2019; Inoguchi et al. 2020; Skalidis et al. 2022), and molecular emission or absorption of other tracers such as CH (Jacob et al. 2019, 2021, 2022), HF (Kavak et al. 2019), and HCO^+ (Liszt et al. 2019; Rybarczyk et al. 2022; Liszt & Gerin 2023b).

The SPLASH survey mapped OH in the galactic plane with the Parkes 64 m telescope and greatly improved our understanding of the distribution of OH in the Galaxy (Dawson et al. 2014). OH was widely detected in all four of the hyperfine structure lines of the ground state. The OH profiles remain difficult to interpret because of the low and uncertain excitation temperatures and nonuniformity and brightness of the continuum temperature toward the inner galaxy, leading to a mix of absorption and emission profiles along the line of sight. However, a large amount of knowledge concerning the anomalous excitation (Petzler et al. 2020, 2021) and catalogs of OH masers have been generated (Dawson et al. 2022). The THOR survey carried out an unbiased OH absorption survey in the first quadrant of the Milky Way with the Karl G. Jansky Very Large Array (VLA; Rugel et al. 2018). This survey detected 59 distinct features against 42 continuum background sources, confirmed the utility of using OH as a tracer of the diffuse H_2, derived physical conditions, and observationally constrained the $N(OH)/N(H_2)$ ratio across a large range of environments.

The observational situation for OH is remarkably different toward the outer galaxy, where the ambient radio continuum temperatures are uniformly low (within 1 K of T_{CMB}). Faint OH emission ($T_{mb} < 0.05$ K) has been repeatedly detected in sensitive blind OH emission surveys, in which the stronger "main" lines (1665/1667 MHz) show the local thermodynamic equilibrium (LTE) intensity ratio of 5:9 (Allen et al. 2012, 2015; Busch et al. 2019). The weaker "satellite" lines (1612, 1720 MHz, 1:1 ratio in LTE) are routinely too faint to detect. In reality, there are commonly departures from the LTE ratio in the satellite lines of interstellar OH (see, e.g., Dawson et al. 2014; Ebisawa et al. 2016, 2019). The 1720 MHz line can sometimes be slightly anomalously emitting (Allen et al. 2015), even if the main lines are in the LTE 5:9 ratio. This behavior may be tracing shocks moving through the ISM leading to compression and increased collisional excitation (Lockett et al. 1998) or be indicative of the slightly anomalous ambient excitation temperatures of the satellite lines, as the SPLASH survey observed widespread diffuse weakly masing 1720 MHz emission, even across entire clouds that are not near supernova remnants (Dawson et al. 2014). Attempts to understand and model the complex excitation and maser phenomenon of the OH molecule have been ongoing for decades (Elitzur & Moshe 1976; Elitzur et al. 1976; Guibert et al. 1978; Dixon & Field 1979; Lockett et al. 1998; Wardle & Yusef-Zadeh 2002; Darling 2007; Hewitt et al. 2008; Lockett & Elitzur 2008; Yusef-Zadeh et al. 2016).

Altogether, OH has been demonstrated to trace the "CO-dark" H_2 in diffuse clouds (Barriault et al. 2010; Cotten et al. 2012; Allen et al. 2015; Engelke & Allen 2018, 2019; Busch et al. 2019), in the envelopes of giant molecular clouds (Wannier et al. 1993), in absorption sight lines across the sky (Li et al. 2015, 2018; Petzler et al. 2023), and, more recently, in a thick "CO-dark" molecular gas "disk" of ultradiffuse H_2 ($n_{H_2} \sim 5 \times 10^{-3}$ cm^{-3}) in the outer galaxy (Busch et al. 2021). Potentially related, broad, faint HCO^+ absorption coincident with H I absorption with no corresponding CO emission or absorption was also recently discovered in several sight lines (Rybarczyk et al. 2022). HCO^+ and OH optical depths have been shown to be tightly correlated in diffuse gas regimes (Liszt & Lucas 1996). A similar discovery of very broad Galactic OH emission and HCO^+ absorption was presented back in 2010 by Liszt et al. (2010) toward one sight line.

We present here, to our knowledge, the first detection of thermal OH emission in another galaxy, M31. We stress that by "thermal," we mean strictly that the 1665:1667 MHz emission is in the 5:9 LTE line ratio; this is sometimes referred to as "quasi-thermal" or "main-line LTE." The 1720 MHz line is undetected, which is consistent with the LTE ratio. As the 1720 MHz line would be 9 times weaker than the 1667 MHz line with the LTE ratio, any such emission would be below our current sensitivity limits. The 1612 MHz line is not recovered because of radio frequency interference (RFI) at the Green Bank Observatory. There is no evidence that the emission is caused by unresolved masing sources in the beam, for which the line strengths would not be in the LTE ratio.

2. Observations and Data

2.1. M31 Blind Pilot Survey Construction

M31 is a natural target for a pilot survey for thermal OH emission due to its proximity; it is the closest Milky Way

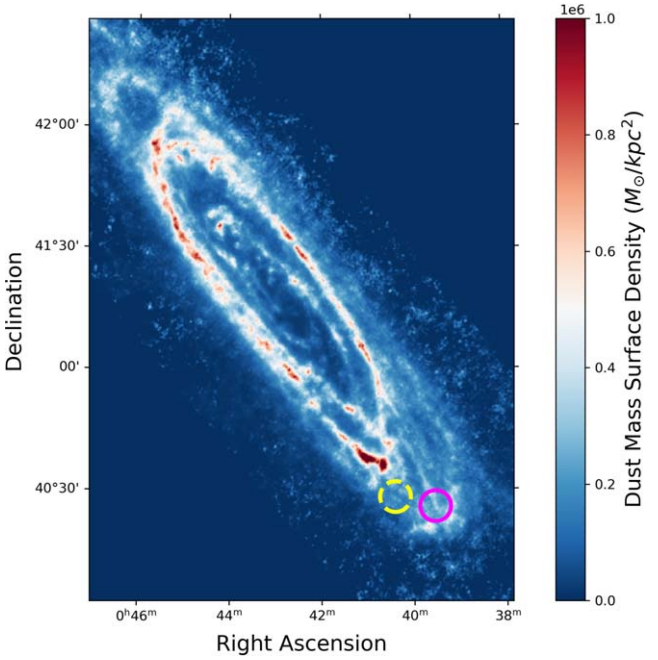

Figure 1. The derived mass surface density map of dust mass in M31 from Draine et al. (2014). The spectroscopic measurement of 18 cm OH discussed in this paper is shown at (J2000) $0^h39^m32^s$+40°26′09″ as a magenta open circle, approximately 62′ from the nucleus, aligned with the major axis of the galaxy. The yellow dashed open circle is the sight line with a nondetection at (J2000) $0^h40^m24^s$ +40°28′11″.

analog and has similar metallicity (Zurita & Bresolin 2012). We chose two positions in M31 to search for OH 18 cm emission, at $\alpha = 0^h39^m32^s$, $\delta = +40°26'09''$ (J2000) and at $\alpha = 0^h40^m24^s$, $\delta = +40°28'11''$ (J2000). Both of these positions are approximately 62′ from the nucleus, corresponding to a distance from the center of ∼13 kpc. This pilot survey was *blind* in the sense that we did not point toward any previously known astronomical object, such as H II regions, supernova remnants, a potential absorption source, etc. The goal was to attempt to observe quiescent diffuse molecular gas on a large physical scale. We did, however, choose these sight lines for several other reasons. First, these sight lines contain relatively bright H I emission, which may increase the likelihood of detecting an OH emission signal at the same coordinates, since recent OH surveys in our Galaxy have demonstrated that H I and OH brightness temperatures are correlated, at least until the H I becomes optically thick (Allen et al. 2012, 2013, 2015; Busch et al. 2021). Second, these two sight lines are spatially separated from the bulk of the CO emission in M31, between 8 and 11 kpc, as presented in Dame et al. (1993), and any OH detections could be indicative of "CO-dark" or "CO-faint" molecular gas at large galactic radii (Wannier et al. 1993; Grenier et al. 2005; Wolfire et al. 2010; Li et al. 2015, 2018), giving us the opportunity to learn more about molecular gas in regions of galaxies where there is an absence of, or very faint, CO emission. Third, we wanted to optimize the detectability of faint OH emission. The continuum temperature at radio wavelengths is typically quite low at large galactic radii, just above T_{CMB}. Generally, this is below the observed range of excitation temperatures of the OH lines (≈4–10 K; Engelke & Allen 2018; Li et al. 2018; Petzler et al. 2023). Inspection of the thermal and nonthermal 6.6 GHz maps show that there are not many candidate H II regions or supernova remnants in the observed region, with most being present in the 10 kpc ring (Fatigoni et al. 2021). Background continuum temperatures above this range could result in a mix of absorption and emission in the main OH lines or no detections at all if the continuum temperatures become approximately equal to the OH excitation temperature.

After 21.26 hr of the exploratory search program, faint OH emission was significantly detected in the first planned sight line ($\alpha = 0^h39^m32^s$, $\delta = +40°26'09''$ (J2000), the magenta aperture marked in Figure 1), which had the higher peak brightness temperature in H I ($T_{peak} = 30$ K). We detected five channels above the 5σ level, covering approximately 20 km s^{-1}. We then spent the rest of the observing time searching for OH in a nearby sight line ($\alpha = 0^h40^m24^s$, $\delta = +40°28'11''$ (J2000), the yellow circle in Figure 1) with the hope of detecting OH in another position. The second sight line had a peak brightness temperature in H I of $T_{peak} = 13$ K. A total of 37.30 hr of integration time was spent on this sight line; there was no statistically significant detection of OH at 1665, 1667, or 1720 MHz in any channels above 2σ. The lack of a secondary OH detection implies that the OH detection in the primary sight line is not an unknown instrumental effect of the telescope or receiver that might have introduced a spurious signal. The spectra of both sight lines are shown in Figure 2.

2.2. Green Bank Telescope Observations

Observations were made with the 100 m Robert C. Byrd Green Bank Telescope (GBT)[1] located in West Virginia within the National Radio Quiet Zone using the Gregorian receiver system operating in the frequency band 1.15–1.73 GHz (*L* band); the observing parameters are summarized in Table 1. Frequencies of transitions of OH and H I observed are summarized in Table 2. The observations took place from 2020 June to 2020 July. The signal is fed to the control by an intermediate-frequency (IF) system. The signal from the IF was copied and directed at four sections of the GBT spectrometer, centered on 1420.40 MHz, 1617.40 MHz, 1666.40 MHz, and 1720.530 MHz. In order to maximize on-signal observing time, we employed in-band frequency-switching by ±2 MHz (O'Neil 2002), such that the expected science signal appears in both switching cycles but in different channel numbers. The spectra from both switching cycles are therefore shifted and inverted before subtraction to average the science signal from both switching cycles. The IF bandwidth was 16.875 MHz, chosen in order to minimize the possibility of harmful radio interference and to make it possible to observe the OH mainline 1665 MHz and 1667 MHz spectra on the same IF band. The frequencies observed also covered the OH satellite lines at 1612 MHz and 1720 MHz, although the 1612 MHz spectra suffer frequent transient baseline ripples from radio interference. We simultaneously observed the H I 21 cm line at 1420 MHz. The data collected for each pointing are made up of a sum of multiple 10 minute scans. The receiver is a single-beam, dual-polarization instrument with an effective system temperature in the range of 16–20 K, depending on the weather, the elevation of the pointing, and background continuum emission. The FWHM of the GBT at 18 cm is 7.′6. The main-beam efficiency of the GBT in this frequency

[1] The Green Bank Observatory is a facility of the National Science Foundation operated under cooperative agreement by Associated Universities, Inc.

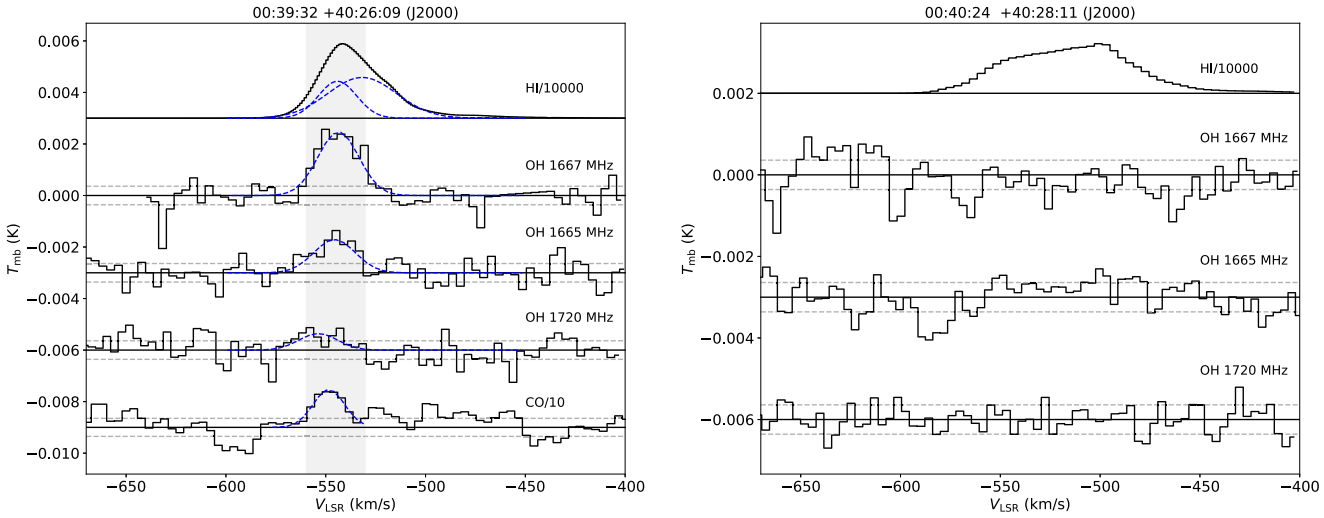

Figure 2. Both sight lines discussed in this paper. OH was detected at the coordinates presented in the left panel. No significant OH signal was detected in the right panel. The observed GBT H I spectra for both positions are also plotted. In the case of the OH lines, the dashed lines correspond to $\pm 1\sigma$ statistical noise, $\sigma T_{\rm mb} \sim 0.36$ mK. We also include the reprocessed CO spectrum in the left panel for comparison to the detected OH 1667 and 1665 MHz lines. The dashed lines for the CO spectrum correspond to $\sigma T_{\rm mb} \sim 3.5$ mK. The gray highlighted region of the spectrum indicates the channels in which OH 1667 is above 1σ. The Gaussian fits discussed in Section 3 are overplotted as blue dashed curves in the left panel, and their fit parameters are reported in Table 3. The H I and CO brightness temperatures are scaled by their indicated values. In the left panel, the offsets for the spectral lines are 0.003, −0.002, −0.006, and −0.009 K for the H I, OH 1665 MHz, OH 1720 MHz, and CO lines, respectively. The right panel is the same except for the H I offset, which is 0.002 K.

Table 1
GBT *L*-band (1.15–1.73 GHz) Observing Parameters

Parameter Description	Value
Project code	AGBT20A_556
Observing dates	2020-06-04 to 2020-07-21
Backend	VEGAS (Prestage et al. 2015)
Polarizations	*X*, *Y* (linear)
Spectral windows	4
Central frequencies (MHz)	1420.40, 1617.40, 1666.40, 1720.53
Pointing source	0114+4823
Bandwith (MHz)	16.875
Spectral resolution (kHz)	1.03
Integration time per spectral dump (s)	5
Beam size (arcmin)	7.6

band is $\eta_{\rm mb} \sim 0.95$, as determined by NRAO staff.[2] This is in good agreement with the value one derives from more recently reported aperture efficiencies for the GBT *L*-band receiver (Boothroyd et al. 2011). The pointing of the telescope was calibrated at the start of each observing session. The GBT project number for the data presented in this paper is AGBT20A_556.

2.3. Archival CO Data

We compare our OH observations with archival CO (1–0) observations taken with the 1.2 m telescope at the Harvard-Smithsonian Center for Astrophysics (CfA; Dame et al. 1993). This CO survey has observed all of M31 out to a radius of at least 15 kpc and has a similar beam size at 8.′7 to the GBT beam at 18 cm OH (7.′6), and it is extremely sensitive, at a $\sigma T_{\rm mb} \sim 18$ mK per 1.3 km s^{-1} channel. This is the only available CO survey of M31 that has overlapping data with our survey; the IRAM CO survey by Nieten et al. (2005) does not extend to the sight lines discussed in this paper.

[2] https://www.gb.nrao.edu/GBT/Performance/PlaningObservations.htm

Table 2
Frequencies of the OH 18 cm ($^2\Pi_{3/2}$, $J = 3/2$) and H I 21 cm Transitions Observed

Species	Transition	ν [MHz]	Sμ^2[a]
OH	$F = 1 - 2$	1612.231	0.79
OH	$F = 1 - 1$	1665.402	4.0
OH	$F = 2 - 2$	1667.359	7.1
OH	$F = 2 - 1$	1720.530	0.79
H I	$F = 1 - 0$	1420.405	⋯

Note.
[a] Sμ^2 is the calculated line strength of the transition, taken from Ebisawa et al. (2016).

2.4. Data Reduction

The H I observations are checked for RFI in each 10 minute scan and then averaged together. A polynomial of order 2 is fit to 100 km s^{-1} on either side of the H I signal and subtracted. The data are smoothed by Gaussian convolution and decimated by five channels; the final velocity resolution is 1 km s^{-1}, and the rms noise per channel is $\sigma T_{\rm mb} \sim 4$ mK. For the OH observations, each 10 minute scan in each linear polarization is reviewed for the presence of interference or other instrumental problems. In general, there are no major sources of RFI near the 1667, 1665, or 1720 MHz lines. Unfortunately, there are large amounts of RFI near the 1612 MHz line, which render it unusable.

Before smoothing and decimation, the noise per channel in the spectrum is approximately 5 mK, and the spectral resolution is 1.88 kHz, corresponding to a velocity resolution of 0.34 km s^{-1}. The resulting noise per channel is $\sigma T_{\rm mb} \sim 0.4$ mK at the final chosen velocity smoothing of 3.88 km s^{-1}, which corresponds to a spectral resolution of 22.24 kHz. The noise levels agree very well with the radiometer equation for the integration times and channel bandwidth, which is good confirmation that we are not overfitting the background in the signal-free baseline regions.

The boundaries for the baseline fitting followed the extent of the H I emission. This was done using the usual baseline fitting procedures in *GBTIDL*, such as *setregion*, *nfit*, and *baseline* (Marganian et al. 2006).

Initial inspection of the CO spectra at our detection position revealed CO coincident with the OH and H I spectra. This was determined to be at least part of the previously discovered Arp Outer Arm S5 in CO in Dame et al. (1993). We smoothed the CO signal with a convolution to a Gaussian kernel and decimated by three channels to a corresponding velocity resolution of 1.7 km s^{-1} using *scipy* (Virtanen et al. 2020). This decreased the resulting rms in the spectra to $\sigma T_{\rm mb} = 3$ mK per 1.7 km s^{-1} channel. The reprocessing demonstrated five channels above 2σ covering 8.5 km s^{-1}, with peak $T_{\rm mb}$ of 17 ± 3 mK. The original CO data and the reprocessed data and Gaussian fit are shown in Figure 4. The extraction position of the spectra is shown on the integrated CO map in Figure 5.

3. Results

Our most significant result is the detection of thermal 18 cm OH emission in another galaxy for the first time, an optically thin radio wavelength tracer of H_2.

3.1. Features of the H I and OH Line Profiles

The observed H I and OH spectra from the GBT are displayed in Figure 2. The peak of the OH emission at 1667 MHz is 2.4 mK, whereas the peak of the 1665 MHz emission is 1.5 mK, close to the expected LTE ratio of the lines. The 1612 MHz line data are unusable due to RFI at Green Bank. We do not detect any emission, or absorption, in the 1720 MHz line. This is expected for LTE conditions: if the 1720 MHz emission were in the LTE ratio (1:5:9:1 for 1612:1665:1667:1720 MHz), then the peak 1720 MHz emission would be buried in the noise, as $T_{\rm mb,1720} = T_{\rm mb,1667}/9 \sim 0.3$ mK. As the rms noise per channel is about 0.4 mK, it is consistent with the LTE interpretation for 1720 MHz emission to be absent at the sensitivity of the observations presented here.

We performed the line integrals directly on the data, which in practice are the sums of channels multiplied by the channel width in km s^{-1}:

$$\mathrm{S(OH)} = \sum T_{\rm mb} \times \Delta V. \quad (1)$$

The statistical error in S(OH) is calculated from the square root of the number of channels ($N_{\rm chan} \sim 100$) in the profile integral times the 1σ baseline rms. The rms is calculated by the *stats* routine in *GBTIDL* between -900 and -600 km s^{-1} (where no signal is present). Typical rms values calculated this way are approximately 0.4 mK, with a slight dependence on the order of baseline polynomial subtracted.

We analyze the H I and OH profiles by fitting Gaussian profile(s) to each line to derive the following line parameters: peak brightness, line width, line center, and their corresponding statistical uncertainties. The Gaussian profiles are fit to the data using *lmfit* (Newville et al. 2014), and the results are reported in Table 3. In the case of the H I profile, two Gaussians are fit, as it seems there is a narrow and broad component. The central velocity and velocity dispersion of the lines are overall similar to each other, indicating that the emission likely arises from gas that is associated with each other. We do note that the broad component of H I is offset from the peak of OH, whereas the narrow component has the same central velocity of the OH. Additionally, there appears to be an extremely faint tail to the H I profile of only a few K between -450 and -500 km s^{-1}, which is likely diffuse H I in the halo of M31 in the sight line.

The integrated line emission values, S(OH), from -600 km s^{-1} to -500 km s^{-1} are 0.056 ± 0.008 K km s^{-1} and 0.039 ± 0.008 K km s^{-1} for the 1667 and 1665 MHz lines, respectively. This corresponds to a signal-to-noise ratio (S/N) of 7 for S(OH_{1667}) and 5 for S(OH_{1665}). In LTE, the ratios between the brightness temperatures vary between 1.8 for optically thin conditions and 1 for infinite optical depths (Tang et al. 2017). The profile integrals of the OH 1665 and 1667 MHz lines appear to be consistent with the LTE ratio, as we calculate $R = \int T_{\rm mb,1667}\, dv / \int T_{\rm mb,1665}\, dv = 1.4 \pm 0.34$.

3.2. Column Densities of H I and OH

The beam-averaged column density of H I can be calculated in the optically thin assumption following, for example, Dickey & Benson (1982). The optically thin assumption leads to a lower limit for the H I column density. On the physical scale discussed in this paper, this is likely a safe assumption, and we are not missing a large opaque fraction of H I. Under assumptions that the spin temperature is much larger than the continuum background at 21 cm and that the gas is characterized by a single temperature, the column density can be calculated directly from the measured brightness temperature, $T_{\rm mb}$,

$$N(\mathrm{H\,I}) = C_{\mathrm{H\,I}} \int T_{\rm mb} dv, \quad (2)$$

where the constant $C_{\mathrm{H\,I}}$ is 1.82×10^{18} cm^{-2} (K km s^{-1})$^{-1}$. The beam-averaged column density, N(OH), along the line of sight is calculated by (e.g., Liszt et al. 2010; Allen et al. 2012, 2015; Busch et al. 2019)

$$N(\mathrm{OH}) = C_{\mathrm{OH},\nu} \left[\frac{T_{\rm ex}}{T_{\rm ex} - T_{\rm bg}} \right] \int T_{\rm mb} dv, \quad (3)$$

where $T_{\rm mb}$ is the main-beam brightness temperature of the OH emission profile from the cloud as observed in one of the 18 cm OH transitions, $T_{\rm ex}$ is the excitation temperature for either the 1667 or 1665 MHz line, $T_{\rm bg}$ is the brightness of the continuum background at 1666 MHz, and the integration over velocity includes all the molecular emission thought to arise in that particular cloud. The constant C_{1667} is 2.257×10^{14} cm^{-2} (K km s^{-1})$^{-1}$ for the 1667 MHz line. The value of C_{1665} for the 1665 MHz line is 4.0×10^{14} cm^{-2} (K km s^{-1})$^{-1}$. The prefactor, $T_{\rm ex}/(T_{\rm ex}–T_{\rm bg})$, is usually called the background correction factor, and a larger contrast between $T_{\rm ex}$ and $T_{\rm bg}$ would lower the uncertainty in the column density correction. Unfortunately, the values for the 18 cm OH lines are usually seen to have excitation temperatures within a few K of the background continuum temperature. The observed range is usually between 4 and 10 K, with the typical values being around 5 K (Liszt & Lucas 1996; Li et al. 2015; Petzler et al. 2023).

We require a reasonable measurement of the background continuum temperature, $T_{\rm bg}$, in order to calculate the OH column density. The usual prescription is to find a continuum survey at a similar frequency, assume a spectral index, and extrapolate to the continuum at 18 cm (Nguyen et al. 2018). We use the 20.5 cm (1462 MHz) Effelsberg+VLA continuum survey of M31 presented in Beck et al. (1998). Inspecting their Figure 4 continuum map, we adopt an average intensity of 1 mJy beam^{-1}. Using the angular resolution of 45″, we

Table 3
Gaussian Fit Parameters and Integrated Line Intensities toward Source M31 OH Detection

Line Description	v_{LSR}[a] (km s^{-1})	FWHM (km s^{-1})	T_{peak}[b] (K)	S[c] (K km s^{-1})	S/N[d]	N[e] (cm^{-2})
H I (narrow)	-544.09 ± 0.22	22.58 ± 0.77	14.32 ± 0.88	344 ± 32	10.75	$6.26 \pm 0.01 \times 10^{20}$
H I (broad)	-531.71 ± 0.71	40.61 ± 0.56	15.80 ± 0.72	683 ± 33	20.69	$1.24 \pm 0.01 \times 10^{21}$
CO($J = 1$–0)	-548.44 ± 0.54	18.63 ± 1.28	0.017 ± 0.004	0.29 ± 0.027	6.9	⋯
OH 1667 MHz	-543.64 ± 0.94	24.15 ± 2.23	0.0024 ± 0.0004	0.057 ± 0.0077	7.3	$3.7 \pm 0.4 \times 10^{13}$
OH 1665 MHz	-545.55 ± 1.84	24.54 ± 4.34	0.0014 ± 0.0004	0.040 ± 0.0079	5.7	$3.8 \pm 0.7 \times 10^{13}$
OH 1720 MHz	-554.71 ± 4.80	22.77 ± 11.32	0.0009 ± 0.0004	0.00059 ± 0.0078	0.076	⋯

Notes.
[a] Fitted Gaussian central velocity.
[b] Fitted Gaussian peak temperature.
[c] Integrated line intensity from -560 to -500 km s^{-1}.
[d] The S/N on S for the given transition.
[e] Calculated column density for $T_{ex} = 5$ K and 6 K for the 1665 and 1667 MHz lines, respectively.

transform this to temperature and then use the following equation to calculate T_{bg} at 18 cm (1666 MHz) assuming a standard spectral index of -2.8 (Nguyen et al. 2018):

$$T_{bg,1666} = T_{CMB} + T_{bg,1462}(1666/1462)^{-2.8}. \quad (4)$$

This results in a T_{bg} of 3.28 K. The 1σ noise in the continuum map near the map edges is stated to be $\approx$150 μJy, and the corresponding error in T_{bg} is negligible.

We have to assume an excitation temperature of the OH lines in the absence of emission/absorption pairs or any further information. The variation of T_{ex} in diffuse clouds has been observationally constrained; the distribution of T_{ex} as presented in Li et al. (2018) is a good starting assumption when we lack coincident absorption and emission profiles. In addition, there was the recent determination of $T_{ex} = 5.1 \pm 0.2$ K in front of the W5 star-forming region using the novel "continuum background" method (Engelke & Allen 2018). Since we detect the OH lines in emission, we know that T_{ex} has to be higher than the continuum temperature in this region, 3.28 K. We take $T_{ex} = 5$ K and 6 K for the 1665 and 1667 MHz lines, respectively, as these lines have been shown to have different excitation temperatures by about 1 K (Engelke & Allen 2018). The approximation of $T_{ex} \gg T_{bg}$ is also a suitable lower limit to the OH column density; as the background correction factor goes to unity, this leaves a floating factor of about a few, depending on the chosen T_{ex}, which the reader should be aware of.

We compute the H I column densities for both fitted Gaussian components separately; we call them broad and narrow, corresponding to their fit velocity widths (FWHM of 40.6 and 22.6 km s^{-1}, respectively). Using the above quantities, the computed H I column density is $N(\mathrm{H\,I})_{broad} = 1.24 \pm 0.01 \times 10^{21}$ cm^{-2} and $N(\mathrm{H\,I})_{narrow} = 6.26 \pm 0.01 \times 10^{20}$ cm^{-2}, where the error is statistical. The column density of OH calculated from the 1667 MHz line is $N(\mathrm{OH}) = 3.7 \pm 0.4 \times 10^{13}$ cm^{-2}. The column density calculated from the 1665 MHz line is $N(\mathrm{OH}) = 3.8 \pm 0.7 \times 10^{13}$ cm^{-2}, which is statistically consistent with the 1667 MHz derived column density. We calculate the abundance ratio of $N(\mathrm{OH})/N(\mathrm{H\,I})$ as 3×10^{-8}, where we use the narrow component of the H I only.

4. Discussion

4.1. Comparing the Gas Mass Traced by H I, CO, and OH

One usage of thermal OH observations would be to quantify how much "CO-dark" gas mass is missed in general by CO observations and in what environments. As CO is going to remain our choice for tracing the bulk of H_2 due to its brightness and abundance, it is imperative to understand all of the systematics associated with it. In the outer galaxy of the Milky Way, OH observations have revealed that 67% of the 81 sight lines in a 1 deg^2 patch of sky contain "CO-dark" molecular gas (Busch et al. 2019). Near cloud edges, the "CO-dark" gas fraction routinely approached 80% (Xu et al. 2016). On kiloparsec scales and between spiral arms, OH emission may be tracing extremely diffuse H_2 that is completely "CO-dark," depending on the interpertation of faint and broad OH profiles in the outer galaxy (Busch et al. 2021).

In order to compare the gas masses traced by H I, CO, and OH in our sight line, we must first adopt suitable conversion factors for each gas tracer. For OH, we need the abundance ratio of $N(\mathrm{OH})/N(\mathrm{H_2})$ to convert our $N(\mathrm{OH})$ to $N(\mathrm{H_2})$. In this diffuse molecular gas regime, we can start by adopting a reasonable estimate for the value for the $N(\mathrm{OH})/N(\mathrm{H_2})$ abundance ratio. We adopt the median literature value of 1×10^{-7} (Liszt & Lucas 1996; Wiesemeyer et al. 2016; Rugel et al. 2018; Jacob et al. 2019). While chemical model calculations tend to produce abundance ratios of varying values over a range of cloud parameter space (8×10^{-9}–4×10^{-6}), observations of the abundance ratio cluster fairly tightly around 1×10^{-7} (Nguyen et al. 2018). Given the size of the resolution element, the median literature value for the ratio is likely a fair approximation because we are averaging over many different environments. This value for the abundance ratio appears to hold for $N(\mathrm{OH})$ values as low as $\sim$a few $\times 10^{12}$ cm^{-2} (Jacob et al. 2019). Most of the literature values were derived for local solar metallicity gas. The metallicity in M31 at the galactic radius discussed here ($\sim$13 kpc) is statistically consistent with solar metallicity (Sanders et al. 2012; Zurita & Bresolin 2012). Note here also that we do not correct by the inclination of the galaxy, so the values are beam-averaged along the line of sight.

As OH is almost always optically thin, we can directly calculate the column density and transform this into a column of H_2. Using the updated Cepheid distance to M31, $D = 761 \pm 11$ kpc (Li et al. 2021), we can calculate the total mass in the enclosed beam via the equation

$$M_{H_2} = N(H_2)\, A_{H_2}\, \mu\, m_H, \quad (5)$$

where $N(H_2)$ is the traced H_2 column. A_{H_2} is the physical area covered by the GBT beam (which is related to the GBT solid

angle and distance to M31 by $A_{H_2} = \Omega\, d^2$), μ is the molecular weight, and m_H is the weight of the hydrogen atom.

We calculate the inferred $N(H_2)$ column density for this sight line from the CO data. The CO-derived $N(H_2)_{CO}$ is $5.8 \pm 0.4 \times 10^{19}\,cm^{-2}$ using the Milky Way value of $X(CO)$ of $2 \times 10^{20}\,cm^{-2}\ (K\,km\,s^{-1})^{-1}$ (Bolatto et al. 2013) with the suggested 30% uncertainty. A slightly higher $X(CO)$ has been suggested for the southern disk of M31 by Leroy et al. (2011), but the Milky Way value is still within the uncertainties of their model. Interestingly, they note that CO-dark H_2 appears to become important in the metallicity range of 12+log(O/H) ~ 8.2–8.4; this is within the range of metallicity suggested for the region covered by our sight line, 12+log(O/H) ~ 8.3 (Zurita & Bresolin 2012).

The mass of H_2 traced by OH is at least 6.7 ± 0.7 (statistical) $\times\ 10^6\ M_\odot$ for the choice of $T_{ex} = 10$ K. The mass can be higher by a factor of a few as we decrease T_{ex} toward T_{bg}. For comparison, the amount of atomic gas mass traced by H I in this same sight line is 3.07 ± 0.01 (statistical) $\times 10^7\ M_\odot$. The mass of H_2 traced by CO, on the other hand, is $1.7 \pm 0.2 \times 10^6\ M_\odot$.

We show the corresponding hydrogen nuclei column density traced by each tracer in Figure 3. The H I spectrum has been scaled by the coefficient $C_{H\,I}$, and the OH spectrum has been scaled by the background correction prefactor, the coefficient C_{1667}, and the abundance ratio of $N(OH)/N(H_2) = 1 \times 10^{-7}$. We used the Galactic $X(CO)$ value suggested from Bolatto et al. (2013). This exercise gives a visualization of the range of "CO-faint" (we say "faint" here as opposed to "dark" because CO is detected) molecular gas that is traced by OH, which is dependent on the assumed T_{ex}.

In the context of star formation in the outskirts of galaxies, the presence of abundant "CO-dark" gas will likely inform new iterations of the global star formation law in the future (Kennicutt 1989; Kennicutt & Evans 2012). Krumholz (2013) pointed out that star formation is observed in the outskirts of nearby spiral galaxies even at extremely low gas surface densities and concluded that the star formation is dominated by diffuse atomic hydrogen. Alternative explanations for this behavior have included ejection of runaway young stars from star-forming clusters that can travel many kiloparsecs during their main-sequence lifetimes due to collisional dynamics (Andersson et al. 2021). Observations of thermal OH emission in the outskirts of galaxies will be crucial to unveiling the diffuse molecular reservoir available for star formation.

4.2. Calibration of N(OH)/N(H_2) by Dust Emission on Kiloparsec Scales

We can use dust data available on M31 to estimate the total neutral gas column density (Nguyen et al. 2018) to calibrate the abundance ratio of $N(OH)/N(H_2)$. The procedure for calibrating the abundance ratio in this way is as follows. First, we obtain an estimate for the dust mass in our observed region (M_d), apply a dust-to-gas mass ratio (M_d/M_H) to obtain an estimate of the total hydrogen gas mass, subtract the contribution of the gas mass by atomic hydrogen (as measured from the N(H I) data), and then assume that the residual amount of gas mass is molecular. We use the dust models of dust emission from Draine et al. (2014) to calculate this quantity. Usually, this calibration is done on much smaller spatial scales than we are discussing here (Nguyen et al. 2018), but since we are averaging over many different environments, we may be averaging over dust systematics as well. The diameter of our resolution element is 1.67 kpc at the distance of M31 (Li et al. 2021), resulting in an area of 2.2 kpc^2. We obtain the dust map shown in Figure 1 and measure the median dust surface mass density in an aperture the size of the GBT beam (7.′6) at our OH detection coordinates. We correct the map to the updated Cepheid distance of $D = 761 \pm 11$ kpc (Li et al. 2021), which introduces a small correction by a few percent.

The resulting median dust surface mass density in the aperture is $2.5 \times 10^5\ M_\odot\,kpc^{-2}$. We use the M_d/M_H prescription from Equation (8) in Draine et al. (2014) for our distance from the center of M31 of 13 kpc. We divide the dust surface mass density by this ratio (0.0079) to obtain the gas surface mass density and further divide by the proton mass to obtain N_H, the column density of hydrogen nuclei. This procedure results in an N_H of $4 \times 10^{21}\,cm^{-2}$. We then calculate the H I column density[3] from the Braun et al. (2009) H I map; the H I column density measured in the same aperture toward the OH detection coordinates is $N(H\,I) = 3 \times 10^{21}\,cm^{-2}$. We subtract this from the column density of the total hydrogen nuclei inferred from dust (N_H) and assume that the rest of the hydrogen nuclei are molecular (H_2). This results in an $N(H_2)$ of $5 \times 10^{20}\,cm^{-2}$.

Finally, we can calibrate the $N(OH)/N(H_2)$ abundance ratio with this result. The corresponding values for $T_{ex} = 5$ and 10 K are 1×10^{-7} and 4×10^{-8}, respectively. These results are consistent with the range of values from the literature and seem to ensure our assumed value of 1×10^{-7}. We also note that the lower value for $N(OH)/N(H_2)$ may be consistent with the interpretation that the metallicity at a galactocentric radius of ~13 kpc for M31 is slightly subsolar, 12+log(O/H) ~ 8.3 (Zurita & Bresolin 2012). However, when considering the scatter on the relation presented in Zurita & Bresolin (2012) and the different calibration methods presented, the metallicity is also consistent with solar values, which most literature values of $N(OH)/N(H_2)$ are reported for.

We should also consider if there should be a correction for opaque H I inside the beam. At large galactic radii, the correction for optically thick H I is expected to be quite low (Koch et al. 2021), and optically thick H I has not been able to reconcile the observed mass of "dark gas" previously (Murray et al. 2018). As a check, a generous 30% correction to N(H I) is used to subtract from the dust results in an $N(H_2)$ of $7.6 \times 10^{19}\,cm^{-2}$ and an abundance ratio of 7×10^{-8}, which is still consistent with literature values of the abundance ratio.

5. Comment on the Relation between H I and Quasi-thermal OH Emission

Recent studies have suggested a correlation between faint optically thin H I and faint optically thin OH emission on large spatial scales (Allen et al. 2012, 2013; Busch et al. 2021). Allen et al. (2012) noticed the main-beam temperatures of H I and OH (1667 MHz) correlating fairly well with each other with the relation $T_{mb}(OH) = 1.5 \times 10^{-4}\ T_{mb}(H\,I)$, with a scatter of 3 mK. This relation seems to hold for $T_{mb}(H\,I) < 60$ K, above which the H I saturates, but the OH brightness temperature continues to rise because it remains optically thin. As discussed in Section 2, this relation guided our exploratory search. The relationship predicts a peak OH signal of 2.6 ± 3 mK in the

[3] Uncorrected for optical depth effects, as the correction from Braun et al. (2009) seemed to overestimate N(H I), as it was incompatible with the gas mass predicted by dust by an order of magnitude.

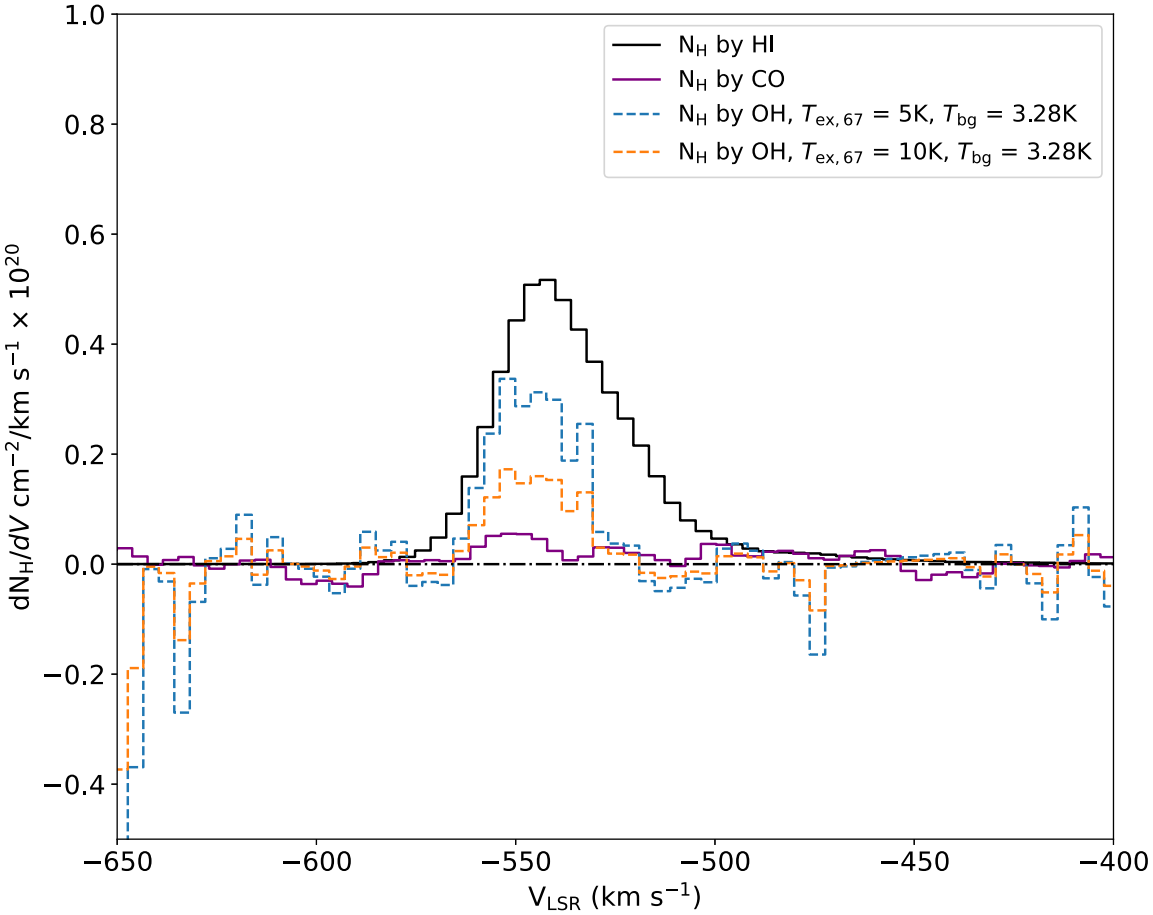

Figure 3. H I, OH, and CO for the sight line discussed in this paper, transformed into hydrogen nuclei (atomic hydrogen for H I, molecular hydrogen for OH and CO) column density per channel (dN_H/dv). We present two choices of T_{ex}, where 5 K is a somewhat standard choice, and 10 K can be considered a lower limit to OH column densities.

sight line without a detection, which is consistent with no detectable signal. The sight line with the OH detection was chosen because the predicted peak signal here is 5.3 ± 3 mK. In building further extragalactic OH searches, this relationship should be consulted and refined. It is especially unknown how this relationship differs with metallicity, for example, which should be a topic of further research.

6. Conclusion

We have detected statistically significant extragalactic emission from faint, thermal (nonmaser, LTE-like) interstellar OH for the first time. The emission is detected in the southern disk of M31 using extremely sensitive GBT observations toward one sight line aligned with the major axis, ∼62′ from the nucleus of the galaxy. A nondetection is also presented, which suggests that the detection presented is not an otherwise unknown instrumental artifact. The velocity structure of the OH closely follows that of the narrow H I component and overlaps several channels of CO emission, implying the existence of molecular gas on the same spatial scale as the atomic gas traced by a portion of the H I. We derived Gaussian line profile parameters from the observed OH and H I data. We also calculated the integrated line intensity profiles of the OH 1665 and 1667 MHz lines and found that they are in the LTE ratio. We compared the OH data with the archival CO data from Dame et al. (1993). When we use dust as a total neutral gas column tracer, we calibrate the $N(\mathrm{OH})/N(\mathrm{H_2})$ abundance ratio between 1×10^{-7} and 4×10^{-8}, respectively, the range arising from the choice of excitation temperature.

Single-dish radio telescopes with ample observing time at centimeter wavelengths (centimeter observations can normally be completed in any weather and any time of day) could systematically map the distribution of the 18 cm OH emission in Local Group galaxies at large galactic radii, where the continuum temperature is only slightly above T_{CMB}. On the other hand, we may also expect to map out the absorption of 18 cm OH toward the inner disks of these galaxies due to increased synchotron emission, which can be interpreted under slightly different assumptions. OH masers, from either OH-IR stars, high-mass star-forming regions, or supernova remnants, would also undoubtedly be detected by any OH survey of Local Group galaxies (Hewitt et al. 2006; Koch et al. 2018). While masers are not generally useful for determining the bulk column density of H_2, they can still tell us about the physical conditions of the ISM given proper modeling (Elitzur et al. 1976; Wardle & Yusef-Zadeh 2002; Ebisawa et al. 2019; Petzler et al. 2020).

Unfortunately, single-beam *L*-band (centimeter) instruments would potentially require a prohibitive amount of time to survey Local Group galaxies at the 18 cm OH lines. New multibeam phased array feeds (e.g., Roshi et al. 2018; Pingel et al. 2021; Burnett et al. 2023) will drastically improve mapping speeds for large single-dish telescopes by orders of magnitude. In the near future, these instruments will be able to

map the distribution of 18 cm OH to trace the "CO-dark" gas, as long as sufficient sensitivities are achieved, $\sigma T_{\rm mb} \sim 1$ mK. High angular resolution and extremely sensitive upcoming observatories like the next-generation VLA (Murphy et al. 2018) and the Square Kilometre Array (Dewdney et al. 2009) should also be explored to study OH emission and OH absorption in the future and will be complementary to the low surface brightness sensitivity of single-dish telescopes.

The amount of molecular gas revealed by the OH observations presented in this paper is significant, between ∼100% and 140% more than the CO in this sight line. These estimates are similar in magnitude to the "CO-dark" gas estimates from γ-ray observations (Grenier et al. 2005) in the Milky Way's halo. It is still unclear if such a correction should be applied to the current CO maps of M31, and more complete observations are warranted, such as a full survey of OH in M31. While CO will undoubtedly remain our brightest general tracer of H_2 in the Galaxy and beyond, mapping the thermal OH emission will drastically improve our understanding of the distribution and mass of the "CO-dark" H_2.

Acknowledgments

We would like to thank the anonymous referees for the helpful comments, insights, and suggestions. M.P.B. is supported by an NSF Astronomy and Postdoctoral Fellowship under the award AST-2202373. We are grateful to the staff at the Green Bank Observatory for their advice and assistance with the operation of the GBT, in particular Karen O'Neil, Jay Lockman, Toney Minter and Pedro Salas. We would like to thank Tom Dame for delivering the M31 CfA CO data in a digital format in private communication. We thank long-time collaborators Dave E. Hogg and Philip Engelke for sharing insightful scientific conversations and discourse. We want to thank and remember our friend, the late Ronald J. Allen, for the mentorship and for the initial conception of this experiment. Our thanks and well wishes go to Jan Allen and the Allen family for their kindness and support. We thank Karin Sandstrom and Josh Peek for comments, suggestions, and guidance. We would also like to thank Joanne Dawson, Anita Hafner, David Neufeld, Michael Rugel, and Arshia Jacob for lively conversations about the OH molecule, its excitation mechanisms, and how to observe it. The authors acknowledge the Interstellar Institute's programs "II4," "II5," and "II6" and the Paris-Saclay University's Institut Pascal for hosting discussions that nourished the development of the ideas behind this work.

Facility: GBT.

Software: astropy (The Astropy Collaboration et al. 2013); scipy (Virtanen et al. 2020), lmfit (Newville et al. 2014).

Appendix
Archival CO Data

In this appendix, we present the archival CO data, both the spectrum (Figure 4) of the original and reprocessed data and the approximate location of the extraction from the original CO data cube (Figure 5), which, in the coordinates used in Dame et al. (1993), are approximately at X, $Y = [-62\farcm4, 1\farcm8]$, where these are offsets from the center of M31. These offsets were calculated by calculating the offset from the Arp Outer Arm S5 to the OH detection source coordinates. The location of the Arp Outer Arm S5 in CO at X, $Y = [-63', 0']$ (Dame et al. 1993, Table 1) is calculated with a directional offset of $63'$ to the J2000 center of M31 at a position angle of $\theta = 37\fdg7$. There is an offset of approximately $\sim 2'$ to the northwest as defined in Dame et al. (1993). While offset from the CO peak at the Arp

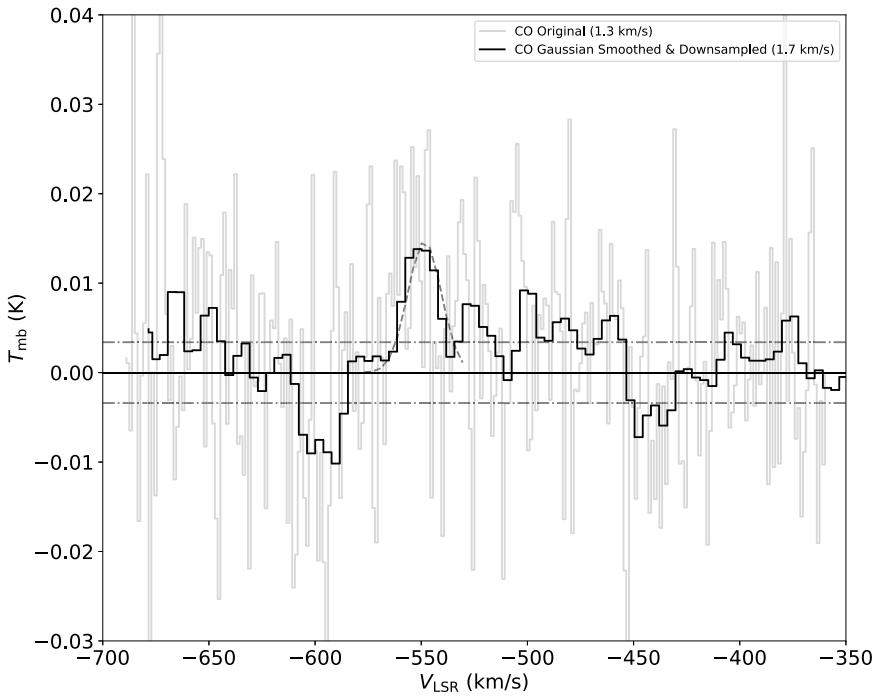

Figure 4. The original CO spectrum extracted from the M31 CfA CO data cube (Dame et al. 1993) with the reprocessed spectrum overplotted. The dashed horizontal black lines represent the 1σ rms of noise of 0.0035 K. The Gaussian fit to the reprocessed data is also overplotted, and the Gaussian fit parameters are reported in Table 3.

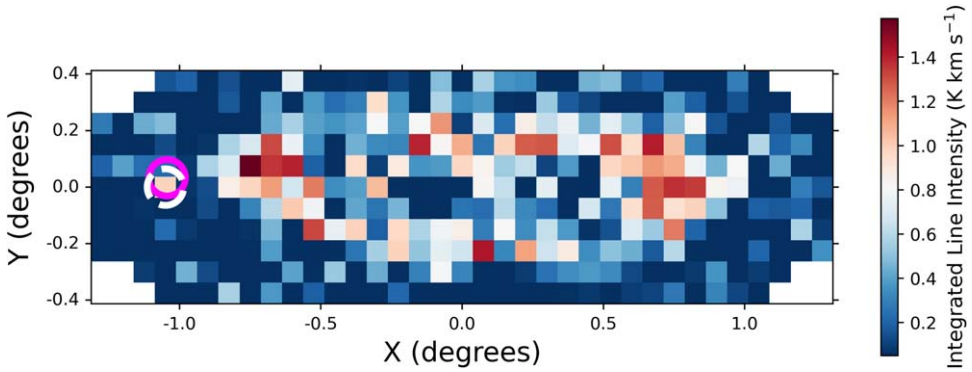

Figure 5. The integrated CO map from Dame et al. (1993), with the position of the OH detection sight line highlighted with the magenta circle. The white dashed circle is the location of the Arp Outer Arm S5, previously discovered in CO, which coincides with our OH detection. The circles are approximately the beam size of the GBT (7.′6), from which the CO spectrum from Figure 4 is extracted. X and Y are rectangular offsets from $\alpha = 0^{h}40^{m}$, $\delta = +41°$ (1950), with X increasing toward the northeast along the major axis of M31 at a position angle of 37.°7.

Outer Arm S5, it still lies within the GBT beam. The results from the Gaussian fit to the CO data are reported in Table 3.

ORCID iDs

Michael P. Busch https://orcid.org/0000-0003-4961-6511

References

Allen, R. J., Hogg, D. E., & Engelke, P. D. 2015, AJ, 149, 14
Allen, R. J., Ivette Rodríguez, M., Black, J. H., & Booth, R. S. 2013, AJ, 145, 85
Allen, R. J., Rodríguez, M. I., Black, J. H., & Booth, R. S. 2012, AJ, 143, 8
Andersson, E. P., Renaud, F., & Agertz, O. 2021, MNRAS, 502, L29
Baan, W. A., Aditya, J. N. H. S., An, T., & Klöckner, H.-R. 2023, MNRAS, 523, 5487
Baan, W. A., Haschick, A., & Henkel, C. 1992, AJ, 103, 728
Baan, W. A., & Haschick, A. D. 1987, ApJ, 318, 139
Barrett, A. H. 1967, Sci, 157, 881
Barriault, L., Joncas, G., Lockman, F. J., & Martin, P. G. 2010, MNRAS, 407, 2645
Beck, R., Berkhuijsen, E. M., & Hoernes, P. 1998, A&AS, 129, 329
Bigiel, F., de Looze, I., Krabbe, A., et al. 2020, ApJ, 903, 30
Bolatto, A. D., Wolfire, M., & Leroy, A. K. 2013, ARAA, 51, 207
Boothroyd, A. I., Blagrave, K., Lockman, F. J., et al. 2011, A&A, 536, A81
Braun, R., Thilker, D. A., Walterbos, R. A., & Corbelli, E. 2009, ApJ, 695, 937
Burnett, M. C., Buck, D., Ashcraft, N., et al. 2023, JAI, 12, 2350002
Busch, M. P., Allen, R. J., Engelke, P. D., et al. 2019, ApJ, 883, 158
Busch, M. P., Engelke, P. D., Allen, R. J., & Hogg, D. E. 2021, ApJ, 914, 72
Chevance, M., Madden, S. C., Fischer, C., et al. 2020, MNRAS, 494, 5279
Combes, F., Gupta, N., Muller, S., et al. 2021, A&A, 648, A116
Cotten, D. L., Magnani, L., Wennerstrom, E. A., Douglas, K. A., & Onello, J. S. 2012, AJ, 144, 163
Curran, S. J., Whiting, M. T., Allison, J. R., et al. 2017, MNRAS, 467, 4514
Dame, T. M., Koper, E., Israel, F. P., & Thaddeus, P. 1993, ApJ, 418, 730
Darling, J. 2007, ApJL, 669, L9
Dawson, J. R., Jones, P. A., Purcell, C., et al. 2022, MNRAS, 512, 3345
Dawson, J. R., Walsh, A. J., Jones, P. A., et al. 2014, MNRAS, 439, 1596
Dewdney, P. E., Hall, P. J., Schilizzi, R. T., et al. 2009, IEEEP, 97, 1482
Dickey, J. M., & Benson, J. M. 1982, AJ, 87, 278
Dickey, J. M., McClure-Griffiths, N., Gibson, S. J., et al. 2013, PASA, 30, e003
Dixon, R. N., & Field, D. 1979, RSPSA, 368, 99
Draine, B. T., Aniano, G., Krause, O., et al. 2014, ApJ, 780, 172
Ebisawa, Y., Inokuma, H., Sakai, N., et al. 2016, ApJ, 815, 13
Ebisawa, Y., Sakai, N., Menten, K. M., & Yamamoto, S. 2019, ApJ, 871, 89
Elitzur, M., Goldreich, P., & Scoville, N. 1976, ApJ, 205, 384
Elitzur, M., & Moshe 1976, ApJ, 203, 124
Engelke, P. D., & Allen, R. J. 2018, ApJ, 858, 11
Engelke, P. D., & Allen, R. J. 2019, ApJ, 874, 49
Fatigoni, S., Radiconi, F., Battistelli, E. S., et al. 2021, A&A, 651, A98
Marganian, P., Garwood, R. W., Braatz, J. A., Radziwill, N. M., & Maddalena, R. J. 2006, in ASP Conf. Ser. 351, Astronomical Data Analysis Software and Systems XV, 351, ed. C. Gabriel et al. (San Francisco, CA: ASP), 512
Goss, W. M. 1968, ApJS, 15, 131
Grenier, I. A., Casandjian, J.-M., & Terrier, R. 2005, Sci, 307, 1292
Guibert, J., Rieu, N. Q., & Elitzur, M. 1978, A&A, 66, 395
Gupta, N., Momjian, E., Srianand, R., et al. 2018, ApJL, 860, L22
Heiles, C. E. 1968, ApJ, 151, 919
Hewitt, J. W., Yusef-Zadeh, F., Wardle, M., Roberts, D. A., & Kassim, N. E. 2006, ApJ, 652, 1288
Hewitt, J. W., Yusef-Zadeh, F., & Wardle, M. 2008, ApJ, 683, 189
Heyer, M., & Dame, T. M. 2015, ARA&A, 53, 583
Inoguchi, M., Hosokawa, T., Mineshige, S., et al. 2020, MNRAS, 497, 5061
Jacob, A. M., Menten, K. M., Wiesemeyer, H., & Ortiz-León, G. N. 2021, A&A, 650, A133
Jacob, A. M., Menten, K. M., Wiesemeyer, H., et al. 2019, A&A, 632, A60
Jacob, A. M., Neufeld, D. A., Schilke, P., et al. 2022, ApJ, 930, 141
Kanekar, N., Carilli, C. L., Langston, G. I., et al. 2005, PRL, 95, 261301
Kavak, U., van der Tak, F. F. S., Tielens, A. G. G. M., & Shipman, R. F. 2019, A&A, 631, A117
Kennicutt, R. C., & Evans, N. J. 2012, ARA&A, 50, 531
Kennicutt, R. C., Jr. 1989, ApJ, 344, 685
Koch, E., Rosolowsky, E., Johnson, M. C., Kepley, A. A., & Leroy, A. 2018, RNAAS, 2, 24
Koch, E. W., Rosolowsky, E. W., Leroy, A. K., et al. 2021, MNRAS, 504, 1801
Krumholz, M. R. 2013, MNRAS, 436, 2747
Leroy, A. K., Bolatto, A., Gordon, K., et al. 2011, ApJ, 737, 12
Li, D., Tang, N., Nguyen, H., et al. 2018, ApJS, 235, 1
Li, D., Xu, D., Heiles, C., Pan, Z., & Tang, N. 2015, PKAS, 30, 75
Li, S., Riess, A. G., Busch, M. P., et al. 2021, ApJ, 920, 84
Liszt, H., & Gerin, M. 2023a, A&A, 675, A145
Liszt, H., & Gerin, M. 2023b, ApJ, 943, 172
Liszt, H., Gerin, M., & Grenier, I. 2019, A&A, 627, A95
Liszt, H., & Lucas, R. 1996, A&A, 314, 917
Liszt, H., Pety, J., & Lucas, R. 2010, A&A, 518, 45
Lockett, P., & Elitzur, M. 2008, ApJ, 677, 985
Lockett, P., Gauthier, E., & Elitzur, M. 1998, ApJ, 511, 235
Madden, S. C., Cormier, D., Hony, S., et al. 2020, A&A, 643, A141
Mebold, N.-Q.-R., Winnberg, U., Guibert, A., & Booth, R, J. 1976, A&A, 52, 467
Murphy, E. J., Bolatto, A., Chatterjee, S., et al. 2018, ASPC, 517, 3
Murray, C. E., Peek, J. E. G., Lee, M.-Y., & Stanimirovic, S. 2018, ApJ, 862, 131
Newville, M., Stensitzki, T., Allen, D. B., & Ingargiola, A. 2014, LMFIT: Non-Linear Least-Square Minimization and Curve-Fitting for Python v0.8.0 Zenodo, doi:10.5281/zenodo.11813
Nguyen, H., Dawson, J. R., Miville-Deschênes, M. A., et al. 2018, ApJ, 862, 49
Nickerson, S., Teyssier, R., & Rosdahl, J. 2019, MNRAS, 484, 18
Nieten, C., Neininger, N., Guelin, M., et al. 2005, A&A, 453, 459
O'Neil, K. 2002, in ASP Conf. Ser. 278, Single-Dish Radio Astronomy: Techniques and Applications, ed. S. Stanimirovic et al. (San Francisco, CA: ASP), 293
Penzias, A. A. 1964, AJ, 69, 146
Petzler, A., Dawson, J. R., Nguyen, H., et al. 2023, PASA, 40, e015

Petzler, A., Dawson, J. R., & Wardle, M. 2020, MNRAS, 497, 4066
Petzler, A., Dawson, J. R., & Wardle, M. 2021, ApJ, 923, 261
Pineda, J. L., Langer, W. D., Velusamy, T., & Goldsmith, P. F. 2013, A&A, 554, A103
Pingel, N. M., Pisano, D. J., Ruzindana, M., et al. 2021, AJ, 161, 163
Planck Collaboration, Ade, P. A. R., & Aghanim, N. 2011, A&A, 536, 16
Prestage, R. M., Bloss, M., Brandt, J., et al. 2015, in USNC-URSI Radio Science Meeting (Joint with AP-S Symp.) (Piscataway, NJ: IEEE), 294
Radhakrishnan, V. 1967, AuJPh, 20, 203
Rogers, A. E., Moran, J. M., Crowther, P. P., et al. 1966, PhRvL, 17, 450
Roshi, D. A., Shillue, W., Simon, B., et al. 2018, AJ, 155, 202
Rugel, M. R., Beuther, H., Bihr, S., et al. 2018, A&A, 618, A159
Rybarczyk, D. R., Stanimirović, S., Gong, M., et al. 2022, ApJ, 928, 79
Sanders, N. E., Caldwell, N., McDowell, J., & Harding, P. 2012, ApJ, 758, 133
Schmelz, J. T., & Baan, W. A. 1988, AJ, 95, 672
Schneider, N., Bonne, L., Bontemps, S., et al. 2023, NatAs, 7, 546
Seifried, D., Haid, S., Walch, S., Borchert, E. M. A., & Bisbas, T. G. 2019, MNRAS, 492, 1465
Skalidis, R., Tassis, K., Panopoulou, G. V., et al. 2022, A&A, 665, A77
Tang, N., Li, D., Heiles, C., et al. 2017, ApJ, 839, 8
The Astropy Collaboration, Robitaille, T. P., Tollerud, E. J., et al. 2013, A&A, 558, A33
Virtanen, P., Gommers, R., Oliphant, T. E., et al. 2020, NatMe, 17, 261
Wannier, P. G., Andersson, B.-G., Federman, S. R., et al. 1993, ApJ, 407, 163
Wardle, M., & Yusef-Zadeh, F. 2002, Sci, 296, 2350
Weaver, H., Williams, D. R. W., Dieter, N. H., & Lum, W. T. 1965, Natur, 208, 29
Weinreb, S., Barrett, A. H., Meeks, M. L., & Henry, J. C. 1963, Natur, 200, 829
Wiesemeyer, H., Güsten, R., Heyminck, S., et al. 2016, A&A, 585, 18
Wilson, R. W., Jefferts, K. B., & Penzias, A. A. 1970, ApJL, 161, L43
Wilson, W. J., & Barrett, A. H. 1968, Sci, 161, 778
Wolfire, M. G., Hollenbach, D., & McKee, C. F. 2010, ApJ, 716, 1191
Wood, P. R., Bessell, M. S., & Whiteoak, J. B. 1986, ApJL, 306, L81
Wood, P. R., Whiteoak, J. B., Hughes, S. M. G., et al. 1992, ApJ, 397, 552
Xu, D., Li, D., Yue, N., & Goldsmith, P. F. 2016, ApJ, 819, 22
Yusef-Zadeh, F., Cotton, W., Wardle, M., & Intema, H. 2016, ApJL, 819, L35
Zheng, Z., Li, D., Sadler, E. M., Allison, J. R., & Tang, N. 2020, MNRAS, 499, 3085
Zurita, A., & Bresolin, F. 2012, MNRAS, 427, 1463